Transient thermal stress intensity factors of bimaterial interface cracks using refined three-fringe photoelasticity

B Neethi Simon, R G R Prasath, and **K Ramesh***
Department of Applied Mechanics, Indian Institute of Technology, Madras, India

The manuscript was received on 11 December 2008 and was accepted after revision for publication on 21 April 2009.

DOI: 10.1243/03093247JSA506

Abstract: Transient thermal stresses of a bimaterial specimen with interface edge cracks subjected to heating along an edge is analysed by refined three-fringe photoelasticity (RTFP). Whole-field, noise-free, fringe order estimation using a single colour image is made possible using RTFP combined with colour adaptation. The stress intensity factors (SIFs) of the interface crack are determined through a multiparameter overdeterministic system of equations by a least-squares approach using experimental data collected automatically. The transient SIFs are found to peak to a higher value than in steady state, and the opening mode is found to be dominant. An increase in thermal load causes the crack to propagate, and this is easily visualized on the basis of quantitative fringe order data available for the whole field. The SIFs of a propagating crack are found to be low. The study shows that the crack propagates easily when the opening mode is dominant.

Keywords: three-fringe photoelasticity, bimaterial interface, stress intensity factor evaluation, transient thermal stresses

1 INTRODUCTION

Most engineering components in use today, such as electronic packages, bimetal thermostats, and even ceramics, consist of materials with different thermal and mechanical properties bonded together. A major concern in such bimaterials is the mismatch in thermal coefficients of expansion of the constituent materials, which gives rise to thermal stress in addition to the stress due to mechanical loading. Bimaterial strips are the simplified models used in the literature for experimental and theoretical analysis of electronic packages and bimetal thermostats [**1**]. Photoelasticity [**1–3**] and moiré interferometry [**4**, **5**] have been used to analyse the steady state thermal stresses in bimaterial strips. During thermal cycling of bimaterial specimens, the induced thermal stresses are predominant near the edges of the interface, which may eventually cause fatigue failure by initiating interface edge cracks [**6**]. The near-tip stress field of a crack can be characterized by the stress intensity factors (SIFs), which are usually expressed as complex numbers for a bimaterial interface crack, as the tensile and shear effects near the crack tip are intrinsically inseparable. For the cases of double-edge cracks in bimaterial specimens subjected to uniform temperature variation [**7**] and uniform heat flux from a surface [**8**], analytical solutions exist for the evaluation of SIFs. In real-life problems, the temperature distribution across the specimen is usually complex, and hence it is necessary to resort to experimental or numerical techniques for their analysis.

In a recent photoelastic study [**9**] on an aluminium–epoxy bimaterial specimen with symmetric interface edge cracks it was observed that even small temperature variations in bimaterial specimens cannot be neglected, as the induced thermal stresses are significant, and a thermomechanical analysis needs to be carried out in the design analysis of bimaterial specimens. Another study [**10**] on an

**Corresponding author: Department of Applied Mechanics, Indian Institute of Technology, Madras, Chennai 600 036, India. email: kramesh@iitm.ac.in*

aluminium–PSM-1 (polycarbonate, Measurements Group Inc., USA) specimen with symmetric interface edge cracks subjected to whole-field cooling by convection showed that, for design, a steady state analysis is sufficient as the steady state SIFs are maximum for this case. Kokini and Smith [**11**] have studied photoelastically an initially cool, edge-heated trimaterial system consisting of a PSM-1–brass interface pasted using an epoxy adhesive. They evaluated the SIFs by using a two-parameter solution and studied the effect of varying the thickness of the adhesive on the SIFs and the strain energy release rate.

Knowledge of the physical phenomenon behind edge heating of bimaterial system is of key importance because, in several engineering applications, components come into contact with one another at different temperatures and are heated or cooled by heat conduction from the surfaces. In this paper, transient thermal analysis of an edge-heated PSM-1–aluminium bimaterial specimen with symmetric interface edge cracks for two different edge heating temperatures is done experimentally using the latest developments of three-fringe photoelasticity (TFP) [**12–14**]. The least-squares approach [**15–17**] is used to evaluate the multiparameters of the stress field surrounding the interface crack.

2 EXPERIMENTAL ANALYSIS

2.1 Choice of bimaterial specimen

Miskioglu *et al.* [**18**] evaluated various photoelastic materials on their application to a transient thermal stress analysis and recommended PSM-1 as the best photothermoelastic material for transient thermal analysis because its material properties remain invariant between −10 and +55 °C. The expansion coefficient of PSM-1 is about six times greater than that of aluminium, while its thermal conductivity and Young's modulus are several orders of magnitude less than those of aluminium (Table 1).

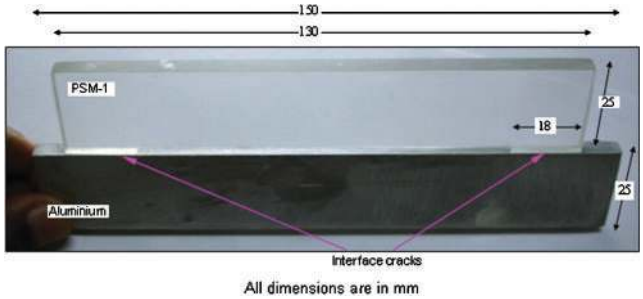

Fig. 1 Aluminium–PSM-1 bimaterial specimen with interface cracks and geometric details indicated (dimensions in mm)

2.2 Preparation of the bimaterial specimen

PSM-1 and aluminium of the same thickness (5.5 mm) are initially cut from the sheets to the dimensions given in Fig. 1. The bonding surfaces are carefully roughened using the commercially available emery sheets for perfect bonding. They are subsequently cleaned using laboratory-grade isopropyl alcohol to remove any traces of dust or grease which would inhibit uniform bonding. The adhesive is prepared by mixing a suitable polyester resin, accelerator, and catalyst. PSM-1 being a polyester-based plastic, the choice of polyester adhesive closely matches a bimaterial interface. Teflon tapes (of 0.075 mm thickness) are placed on the edges to form two symmetric edge cracks each of 18 mm length, with a thin coat of silicon grease applied on them for easy removal after curing. The adhesive is applied on the surfaces to be bonded, light pressure is applied, and the specimen is allowed to set for 12 h at room temperature (30 °C). After curing, the Teflon tape is removed, forming the two interface edge cracks as indicated in Fig. 1.

2.3 Recording of transient stress fields

Figure 2 is a schematic representation of the experimental set-up for the circular polariscope dark-field optical arrangement. A temperature-controlled heating plate is maintained at a temperature of 50 °C.

Table 1 Material properties

Specimen number	Property	Units	Aluminium	PSM-1 [**18**]
1	Density, ρ	g/cm^3	2.823	1.17
2	Expansion coefficient, α	°C^{-1}	22.7×10^{-6}	146×10^{-6}
3	Thermal conductivity, k	W/(m K)	142	0.365
4	Specific heat capacity, C_P	J/(g °C)	0.963	1.1052
5	Young's modulus, E	GPa	71	2.39
6	Poisson's ratio, ν	—	0.33	0.38
7	Material stress fringe value	N/(mm fringe)	—	7

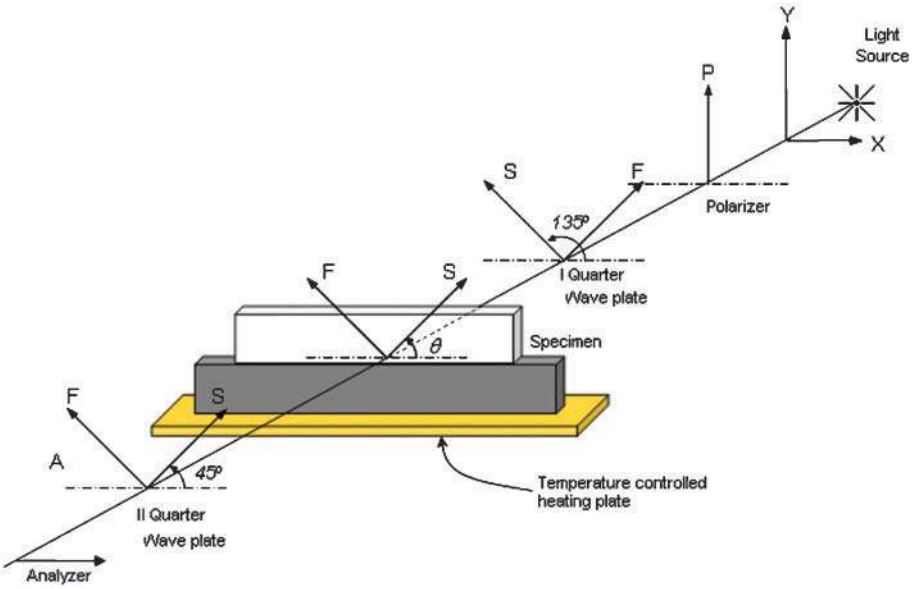

Fig. 2 Circular polariscope dark-field arrangement

The bottom face of the aluminium part of the bimaterial specimen is suddenly placed on the heating plate, and the specimen is heated by surface conduction. Meanwhile, the specimen loses heat by convective heat transfer from the exposed faces to the ambient. The transient phenomenon until thermal equilibrium is achieved is of interest. The dark-field isochromatics is automatically recorded at time intervals of 15 s successively using a colour 3CCD camera (Sony XC-003) with a resolution of 752×576 pixels, by a software module developed in-house using VC++, until steady state is reached (about 12 min). The experimental dark-field isochromatics for a few time steps is shown in Fig. 3. From the experimental images it can be seen that the fringes are concentrated at the crack tip. In the central zone of the bimaterial specimen, the fringes are observed to be parallel to the interface. This is because the thermal load forces the specimen to undergo bending.

On careful observation of different time-step images it can also be seen that the fringe order at the crack tip rises quickly (Fig. 3(d)) and then drops slowly (Fig. 3(g)), especially near the crack tip. This can be explained as follows. As soon as the specimen is kept on the hot plate, the aluminium is heated from the bottom face by surface conduction, and very quickly the temperature becomes fairly uniform because of its high thermal conductivity. Although the thermal coefficient of aluminium is lower than that of PSM-1, aluminium heats to a higher temperature and expands more in relation to PSM-1, causing the crack to open. Because the thermal conductivity of PSM-1 is extremely low, it expands slowly, only after the heat flows through the aluminium. Because of the high expansion coefficient, even the small temperature rise occurring in the PSM-1 portion causes it to expand considerably, and the magnitudes of stresses present along the bond begin to decrease. About 12 min after the commencement of the experiment, the temperature field of the specimen and the thermal stresses within it approach a steady state.

2.4 Total fringe order evaluation using refined three-fringe photoelasticity combined with colour adaptation

Three-fringe photoelasticity (TFP) can give the total fringe order from a single colour isochromatic fringe field by suitably comparing the colour with a calibration specimen [**12**]. For any test data point, an error term e is defined as [**19**]

$$e = \sqrt{(R_e - R_c)^2 + (G_e - G_c)^2 + (B_e - B_c)^2} \tag{1}$$

where subscript 'e' refers to the experimentally measured values for the data point, and subscript 'c' denotes the values in the calibration table. The calibration table is to be searched until the error e is a minimum. For the R_c, G_c, and B_c values thus determined, the calibration table provides the total fringe order.

It has been found that using only the colour information for total fringe order identification can

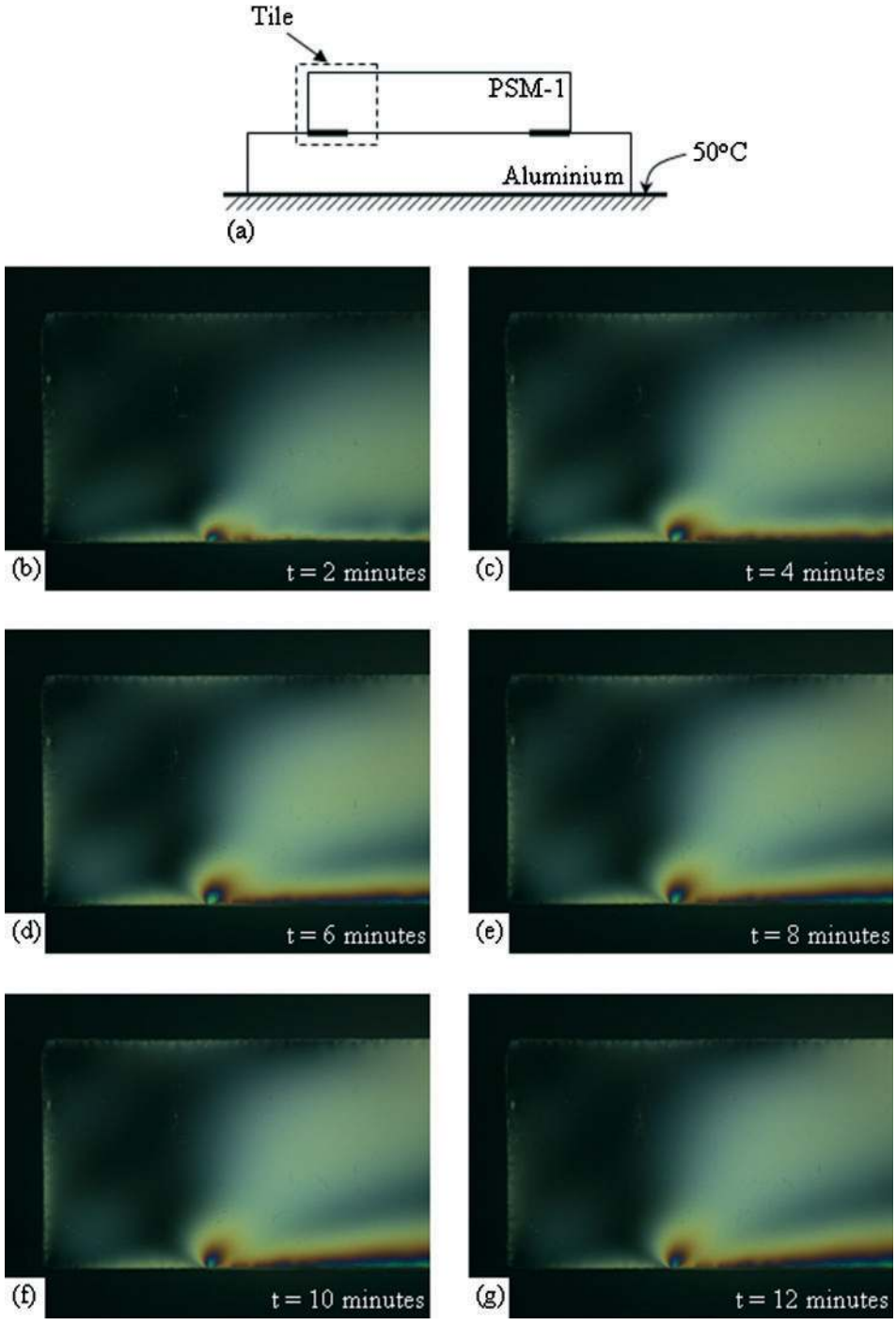

Fig. 3 (b) to (g) Transient dark-field isochromatics recorded in colour (but appearing in black and white in the print version) for an aluminium–PSM-1 bimaterial specimen kept on a hot plate at 50 °C for the rectangular tile shown in (a)

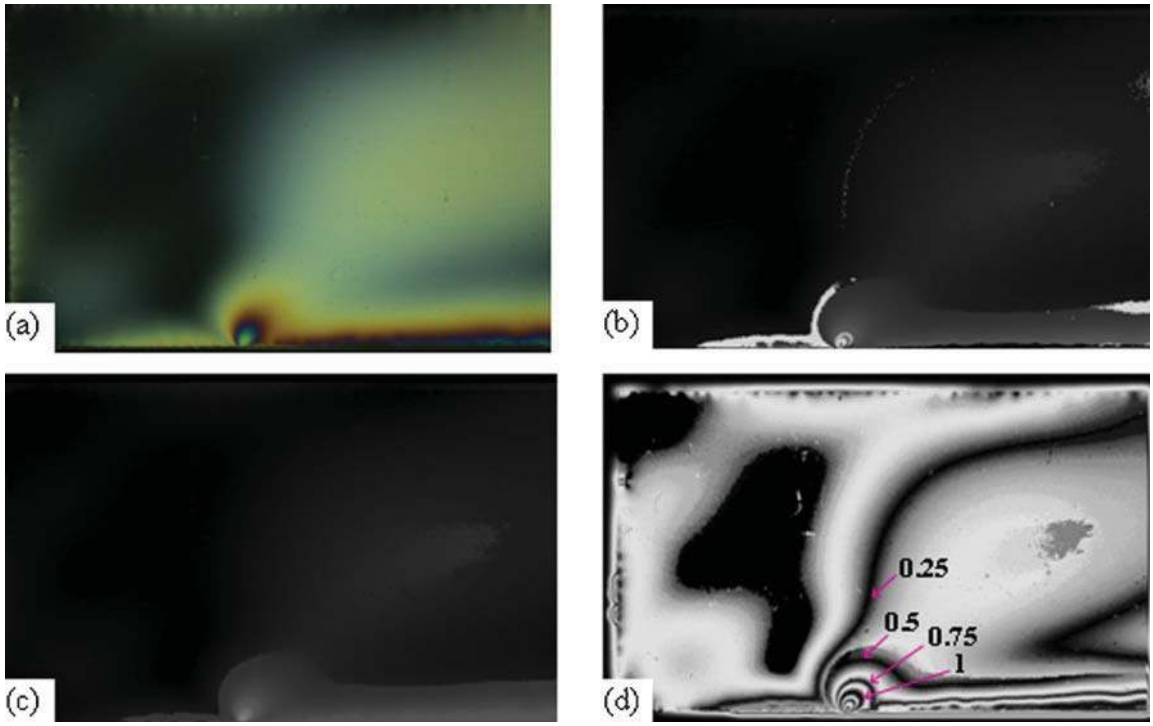

Fig. 4 (a) Dark-field image recorded in colour (but shown in black and white in the print version). Image representation of total fringe order: (b) TFP using equivalent table to accommodate tint variation; (c) refined TFP applied for (b); (d) composite-field image generated after data smoothing

lead to error, and in refined three-fringe photoelasticity (RTFP) [**13**, **20**] the error equation has an additional term and is defined as

$$e = \sqrt{(R_e - R_c)^2 + (G_e - G_c)^2 + (B_e - B_c)^2 + (N_p - N)^2 \times K^2} \quad (2)$$

where N_p is the fringe order obtained for the neighbourhood pixel to the point under consideration, and N is the fringe order at the current checking point of the calibration table. The additional term assures fringe order continuity, and the multiplication factor K is used to have control on the performance of equation (2). The magnitude of K has to be selected iteratively, and a value of 100 is found to be suitable for this problem.

Owing to the difference in ambient lighting, ageing of the polymer, annealing of the specimen, etc., there could be tint variation in the calibration specimen and the specimen under test. To overcome this difficulty of tint variation, Madhu *et al.* [**14**] recently proposed a colour adaptation technique in TFP. In this, an equivalent calibration table is prepared for the specimen under test from the existing calibration table by modifying the RGB intensities for each colour as [**14**]

$$R_{mi} = \frac{R_{ze}}{R_{zc}} R_{ci}, \quad G_{mi} = \frac{G_{ze}}{G_{zc}} G_{ci}, \quad B_{mi} = \frac{B_{ze}}{B_{zc}} B_{ci} \quad (3)$$

where R_{mi}, G_{mi}, and B_{mi} are the RGB values in the modified calibration table in the ith row, R_{ci}, G_{ci}, and B_{ci} are the RGB values in the original calibration table in the ith row, and R_{ze}, G_{ze}, B_{ze} and R_{zc}, G_{zc}, B_{zc} are the no-load bright-field intensities of the specimen under test and the calibration specimen respectively.

The data extraction procedure is explained for one of the dark-field circular polariscope images recorded 6 min after the start of the experiment (Fig. 4(a)). Figure 4(b) shows the image representation of total fringe order variation obtained by using an equivalent calibration table generated for the specimen under test using the colour adaptation technique. Figure 4(c) shows the image representation of the total fringe order by applying RTFP to Fig. 4(b), which shows that the image is free from noise. This is further smoothed by an outlier smoothing algorithm [**21**] using a span width of 3 pixels and a linear polynomial for curve fitting. A *composite-field* image consisting of bright, dark, and

mixed-field [**17**] fringes (fringes in steps of 0.25) is generated from the whole-field fringe order data for ease of data extraction for SIF studies.

2.5 SIF evaluation using the least-squares method

Ravichandran and Ramesh [**17**] have simplified the stress field equations of Deng [**22**] for use by experimentalists, and the Cartesian stress components of the stress field equation for the top half-plane of an interface crack tangential to a bimaterial joint (Fig. 5) loaded at the boundary are given as

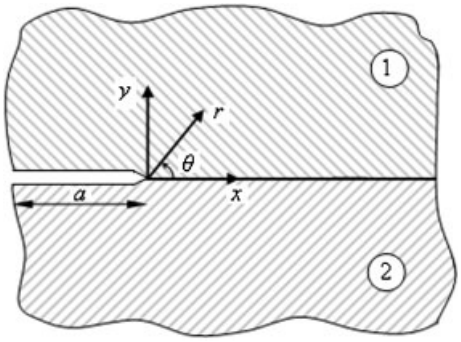

Fig. 5 Schematic of the bimaterial interface crack

$$
\begin{Bmatrix} (\sigma_{xx})_1 \\ (\sigma_{yy})_1 \\ (\tau_{xy})_1 \end{Bmatrix} = \sum_{n=0,2,4}^{\infty} \frac{K_{\mathrm{I}n}}{Q} r^{(n-1)/2} \begin{Bmatrix} S\{3\cos[(\frac{n-1}{2})\theta - \varepsilon \ln \frac{r}{L}] - (n-1)\sin\theta \sin[(\frac{n-3}{2})\theta - \varepsilon \ln \frac{r}{L}] \\ S\{\cos[(\frac{n-1}{2})\theta - \varepsilon \ln \frac{r}{L}] + (n-1)\sin\theta \sin[(\frac{n-3}{2})\theta - \varepsilon \ln \frac{r}{L}] \\ S\{-\sin[(\frac{n-1}{2})\theta - \varepsilon \ln \frac{r}{L}] - (n-1)\sin\theta \cos[(\frac{n-3}{2})\theta - \varepsilon \ln \frac{r}{L}] \end{Bmatrix}
$$

$$
\begin{Bmatrix} +2\varepsilon \sin\theta \cos[(\frac{n-3}{2})\theta - \varepsilon \ln \frac{r}{L}]\} - \frac{1}{S}\cos[(\frac{n-1}{2})\theta + \varepsilon \ln \frac{r}{L}] \\ -2\varepsilon \sin\theta \cos[(\frac{n-3}{2})\theta - \varepsilon \ln \frac{r}{L}]\} + \frac{1}{S}\cos[(\frac{n-1}{2})\theta + \varepsilon \ln \frac{r}{L}] \\ -2\varepsilon \sin\theta \sin[(\frac{n-3}{2})\theta - \varepsilon \ln \frac{r}{L}]\} + \frac{1}{S}\sin[(\frac{n-1}{2})\theta + \varepsilon \ln \frac{r}{L}] \end{Bmatrix}
$$

$$
+ \sum_{n=1,3,5}^{\infty} \frac{K_{\mathrm{I}n}}{R} r^{\frac{n-1}{2}} \begin{Bmatrix} 4\cos(\frac{n-1}{2})\theta - (n-1)\sin\theta \sin(\frac{n-3}{2})\theta \\ (n-1)\sin\theta \sin(\frac{n-3}{2})\theta \\ -2\sin(\frac{n-1}{2})\theta - (n-1)\sin\theta \cos(\frac{n-3}{2})\theta \end{Bmatrix}
$$

$$
+ \sum_{n=0,2,4}^{\infty} \frac{K_{\mathrm{II}n}}{Q} r^{\frac{n-1}{2}} \begin{Bmatrix} S\{3\sin[(\frac{n-1}{2})\theta - \varepsilon \ln \frac{r}{L}] + (n-1)\sin\theta \cos[(\frac{n-3}{2})\theta - \varepsilon \ln \frac{r}{L}] \\ S\{\sin[(\frac{n-1}{2})\theta - \varepsilon \ln \frac{r}{L}] - (n-1)\sin\theta \cos[(\frac{n-3}{2})\theta - \varepsilon \ln \frac{r}{L}] \\ S\{\cos[(\frac{n-1}{2})\theta - \varepsilon \ln \frac{r}{L}] - (n-1)\sin\theta \sin[(\frac{n-3}{2})\theta - \varepsilon \ln \frac{r}{L}] \end{Bmatrix}
$$

$$
\begin{Bmatrix} +2\varepsilon \sin\theta \sin[(\frac{n-3}{2})\theta - \varepsilon \ln \frac{r}{L}]\} + \frac{1}{S}\sin[(\frac{n-1}{2})\theta + \varepsilon \ln \frac{r}{L}] \\ -2\varepsilon \sin\theta \sin[(\frac{n-3}{2})\theta - \varepsilon \ln \frac{r}{L}]\} - \frac{1}{S}\sin[(\frac{n-1}{2})\theta + \varepsilon \ln \frac{r}{L}] \\ +2\varepsilon \sin\theta \cos[(\frac{n-3}{2})\theta - \varepsilon \ln \frac{r}{L}]\} + \frac{1}{S}\cos[(\frac{n-1}{2})\theta + \varepsilon \ln \frac{r}{L}] \end{Bmatrix}
$$

$$
+ \sum_{n=1,3,5}^{\infty} \frac{K_{\mathrm{II}n}}{R} r^{\frac{n-1}{2}} \begin{Bmatrix} 2\sin(\frac{n-1}{2})\theta + (n-1)\sin\theta \cos(\frac{n-3}{2})\theta \\ 2\sin(\frac{n-1}{2})\theta - (n-1)\sin\theta \cos(\frac{n-3}{2})\theta \\ -(n-1)\sin\theta \sin(\frac{n-3}{2})\theta \end{Bmatrix} \tag{4}
$$

where

$$
Q = 2\sqrt{2\pi}\cosh\pi\varepsilon, \quad R = \sqrt{2\pi}\,(1+w),
$$

$$
S = \mathrm{e}^{-\varepsilon(\pi-\theta)}, \quad \varepsilon = \frac{1}{2\pi}\ln\frac{G_2\kappa_1 + G_1}{G_1\kappa_2 + G_2},
$$

$$
w = \frac{(1+\kappa_1)G_2}{(1+\kappa_2)G_1}, \quad \kappa_i = \frac{3-\nu_i}{1+\nu_i}, \quad i = 1, 2
$$

K_{In} and K_{IIn} are the stress field parameters, ε is the bimaterial constant, L is the characteristic length, and G_i and ν_i are respectively the shear moduli and the Poisson's ratios of the two materials ($i = 1,2$).

The least-squares method described in reference [**17**] is used to evaluate iteratively the multiparameters governing the stress field. Although data can be collected anywhere from the fringe field, for easy convergence it has been proposed [**17**] that the fringe order and the corresponding positional coordinates need to be collected such that, when plotted, they capture the basic geometric features of the fringe field. As data need to be collected for each time step, manual data collection along the thinned fringe skeletons would not only be erroneous but

Table 2 Summary of stress field parameters evaluated from field data

Stress field parameters	Two-term	Three-term	Four-term	Five-term	Six-term
K_I (MPa$\sqrt{m}$)	**0.091**	**0.072**	**0.069**	**0.069**	**0.069**
K_{II} (MPa$\sqrt{m}$)	**0.054**	**0.042**	**0.042**	**0.040**	**0.036**
K_{I0} (MPa mm$^{1/2}$)	2.880	2.278	2.169	2.167	2.167
K_{I1} (MPa)	0.069	−7.653	−7.662	−6.164	−2.909
K_{I2} (MPa mm$^{-1/2}$)		0.470	0.492	0.879	1.925
K_{I3} (MPa mm^{-1})			−0.504	−0.368	−0.605
K_{I4} (MPa mm$^{-3/2}$)				−0.029	−0.285
K_{I5} (MPa mm^{-2})					0.334
K_{II0} (MPa mm$^{1/2}$)	1.693	1.329	1.329	1.265	1.138
K_{II1} (MPa)	0.000	0.000	0.000	0.000	0.000
K_{II2} (MPa mm$^{-1/2}$)		0.107	−0.056	−0.045	0.042
K_{II3} (MPa mm^{-1})			1.857	0.241	−9.943
K_{II4} (MPa mm$^{-3/2}$)				0.004	0.066
K_{II5} (MPa mm^{-2})					0.238
Convergence error	**0.069**	**0.062**	**0.036**	**0.036**	**0.021**

tedious as well. Hence, automated data collection [**23**] is implemented. In this, the *composite-field* image is scanned at intervals of 1°, and only those points that are closer ($N \pm 0.02$) to fringe orders of 0.25, 0.5, 0.75, and so on, that lie in the range $0.05 < r/a < 0.65$, are selected for SIF evaluation. The automated data collection software has an interactive module to remove outliers. The zone for SIF evaluation is problem dependent and varies slightly from one time step to another.

For the sake of illustration, the fringe field recorded in Fig. 4 is used. The fringe orders and positional coordinates of about 336 data points are selected automatically in the range $0.06 < r/a < 0.59$, which are used for SIF evaluation using the least-squares method. As the number of parameters involved in characterizing the stress field are not known *a priori*, the iteration is started with two parameters each of the K_I and K_{II} series. The iteration is stopped using the fringe order error minimization criteria [**17**]. Using the solution of the parameters thus obtained as starting values, the number of parameters in each series needs to be iteratively increased until the convergence error obtained is of the order of 0.05 or less [**17**]. The reconstructed *composite fringe field* images (having a fringe order of 0, 0.25, 0.5, 0.75, etc.), with data points echoed for the two-term, three-term, four-term, five-term, and six-term solutions, are given in Figs 6(a) to (e) respectively. The stress field parameters are summarized in Table 2. Although for the present problem the four-parameter solution (Fig. 6(c)) itself satisfies the convergence criteria, it is seen that the six-parameter solution (Fig. 6(e)) matches the fringe field very well. From the six-parameter solution, the values of K_I and K_{II} are 0.064 and 0.036 MPa $\sqrt{m}$ respectively; thereafter, they drop gradually as steady state is reached because the magnitude of stresses along the bond decreases owing to the reduced temperature gradient at the interface.

From the recorded dark-field isochromatics for every time step, the total fringe order variation is obtained using RTFP, and the SIFs are evaluated from the data collected. Note that the crack tip location remains unchanged for every time step. The variations in the SIFs with time are plotted as a graph in Fig. 7, which clearly indicates that the opening mode is dominant. The peaks in K_I and K_{II} occur after about 7 min and 2 min 45 s respectively.

2.6 Effect of increase in the edge heating temperature

It was of interest to study the effect of increasing the temperature of the hot plate on the transient thermal stresses and SIFs. One general observation was that, when the temperature of the hot plate was increased, the crack propagated. A temperature of 60 °C was selected to capture this behaviour because random temperature checks had confirmed that, at this hot-plate temperature, the temperature of the PSM-1 portion was well within 55 °C, which is the maximum temperature recommended by Miskioglu *et al.* [**18**]. The transient dark-field isochromatics is recorded at 15 s intervals using a 3CCD camera, as described earlier. The dark-field isochromatics recorded for a few time steps is shown in Fig. 8.

From the experimental dark-field isochromatics, the total fringe order variation for each time step is obtained for the whole field, as described earlier. The variation in fringe order for a line AB at 2 mm from the interface is plotted as a graph for a few time steps for both edge heating temperatures (Fig. 9). When the temperatures of the bottom face of aluminium are kept at 50 and 60 °C, the peak in fringe order

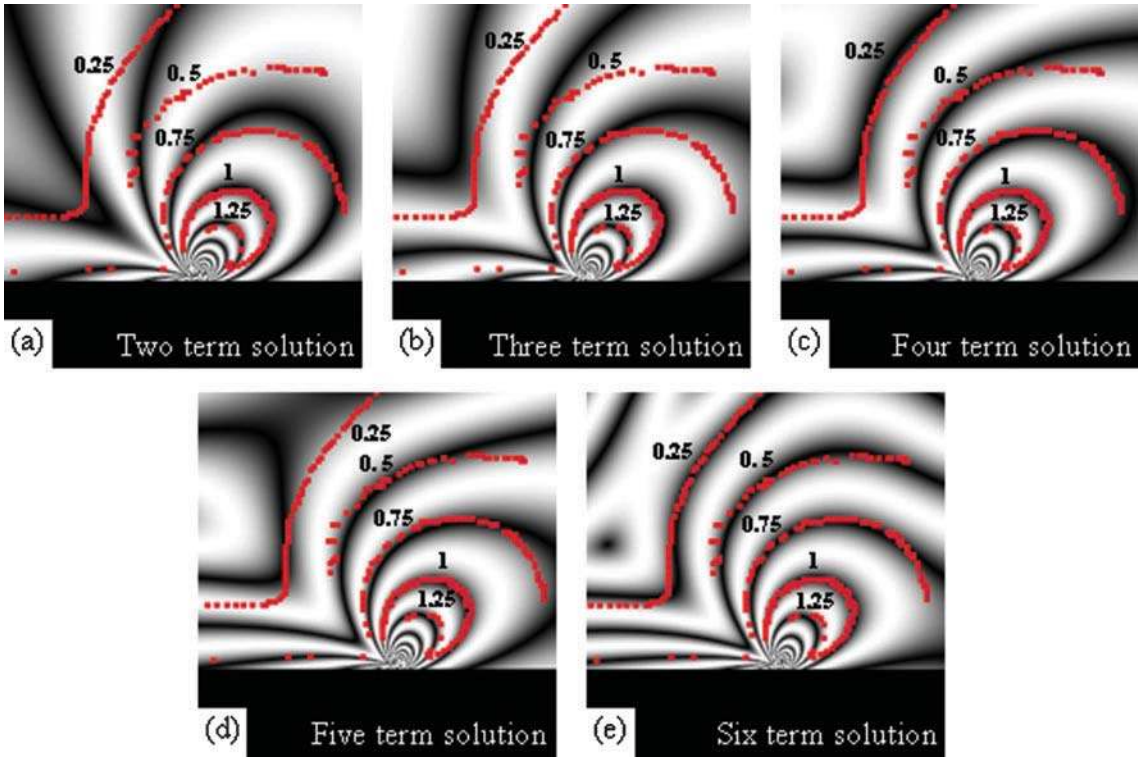

Fig. 6 *Composite-field* image reconstructed from stress field parameters evaluated using the least-squares method with data points echoed

value near the crack tip starts to drop after 6 min (Fig. 9(a)) and 4 min (Fig. 9(b)) respectively. At 50 °C, the locations of the peaks for various time steps remain constant (Fig. 9(c)), but for the 60 °C case the peaks shift to the right steadily after 4 min (Fig. 9(d)), indicating that the crack has begun to propagate. In the 12 min after the start of the experiment for the 60 °C case, the crack was found to propagate by 1.5 mm.

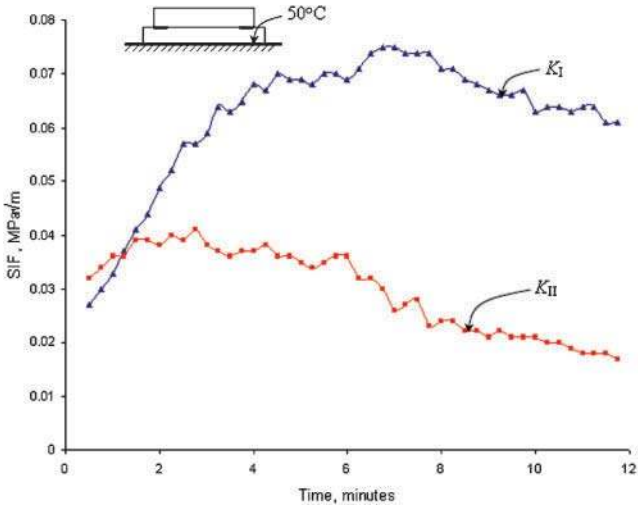

Fig. 7 Graph showing the variation in SIFs for a bimaterial specimen with time when the bottom face of the aluminium is maintained at 50 °C

2.7 SIF evaluation for a propagating crack

The SIFs are evaluated using the fringe order data obtained from RTFP and positional coordinates with respect to the crack tip for each time step. Up to about 4 min 15 s, the crack tip location remains constant. Thereafter, for each time step, the location of the crack tip is determined from a zoomed experimental image by trial and error (Fig. 10), and the new crack tip origin is used for data collection. Transient SIFs are evaluated using the least-squares method, as described earlier, and their variation with time is plotted as a graph (Fig. 11). Based on the shifting crack tip data, the crack propagation with time is determined, and is also plotted as a graph in Fig. 11.

The peaks in K_I and K_{II} occur earlier than the 50 °C case, at 3 min 30 s and at 2 min respectively. It can be seen from the graph that K_{II} drops gradually after 2 min owing to the reduced shear stresses generated between aluminium and PSM-1 as steady state is approached, as observed in the 50 °C case. However, after 4 min 15 s, the SIFs (in particular K_{II}) drop

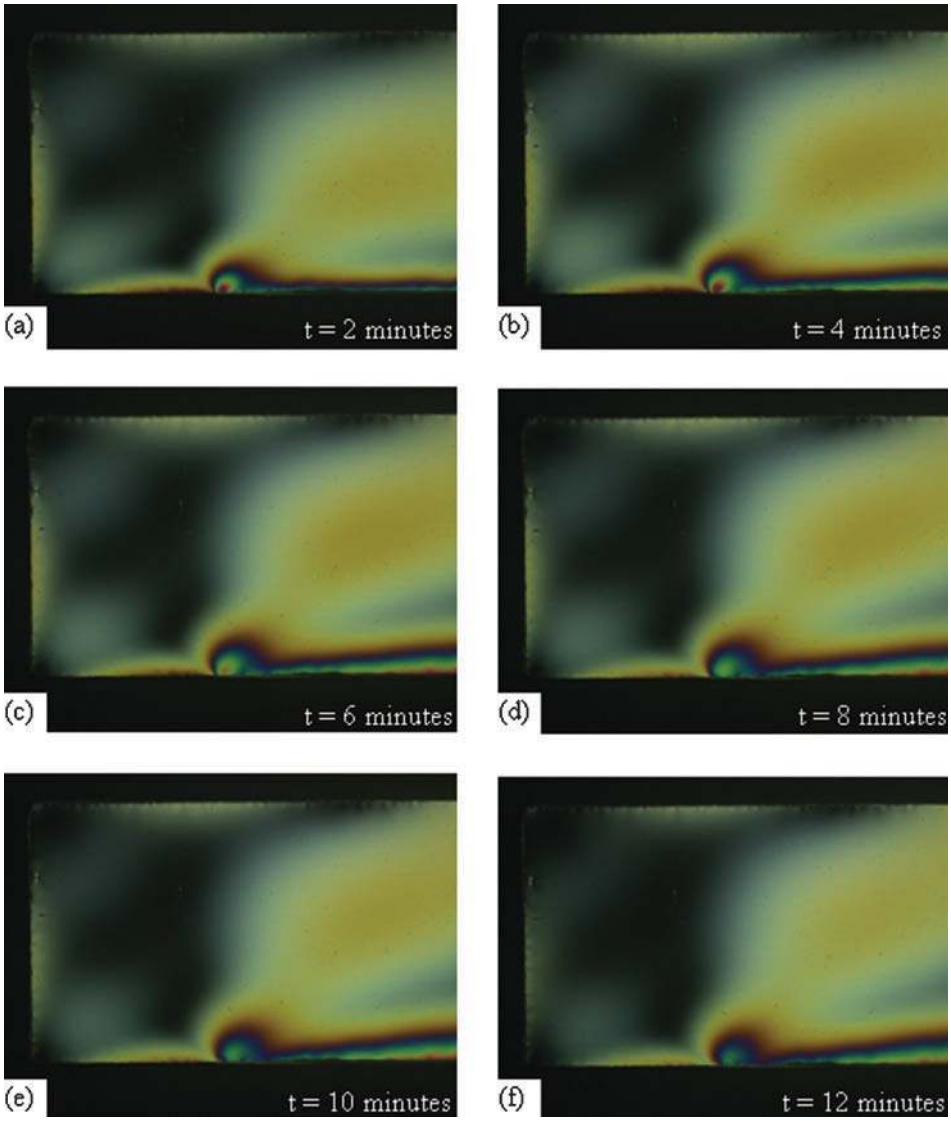

Fig. 8 Transient dark-field isochromatics recorded in colour (but appearing in black and white in the print version) for an aluminium–PSM-1 bimaterial specimen kept on a hot plate at 60 °C for the rectangular tile shown in Fig. 3(a)

rapidly. This sudden drop is different, and from the crack propagation curve it is clear that the crack begins to propagate at this point. The graph shows that the crack propagation is not continuous but intermittent. For reinitiation of the crack (such as at 5 min 15 s), the SIFs have to change in order to force the crack to propagate. Eventually, the value of K_{II} decreases to very near zero.

3 DISCUSSION ON RESULTS

A comparison of the peak values of SIFs for the two different temperature conditions showed that the peak occurs much earlier when the aluminium edge is at 60 °C than when it is at 50 °C (Table 3). In edge heating of the bimaterial specimen, the opening mode is found to be dominant. From a recent study on transient thermal stresses in the same aluminium–PSM-1 specimen subjected to whole-field convection cooling (cooling by convection in still air from a slightly elevated bonding temperature) it was observed that only at steady state were the stresses maximum and K_{II} dominant [**10**]. Although the modulus of the complex SIF, $|K|$, and K_{II} were much higher, the crack did not propagate. However, K_I was lower than the present case. It can therefore be inferred that, for bimaterial specimens of this nature, the dominance of the opening mode causes the crack to propagate more easily.

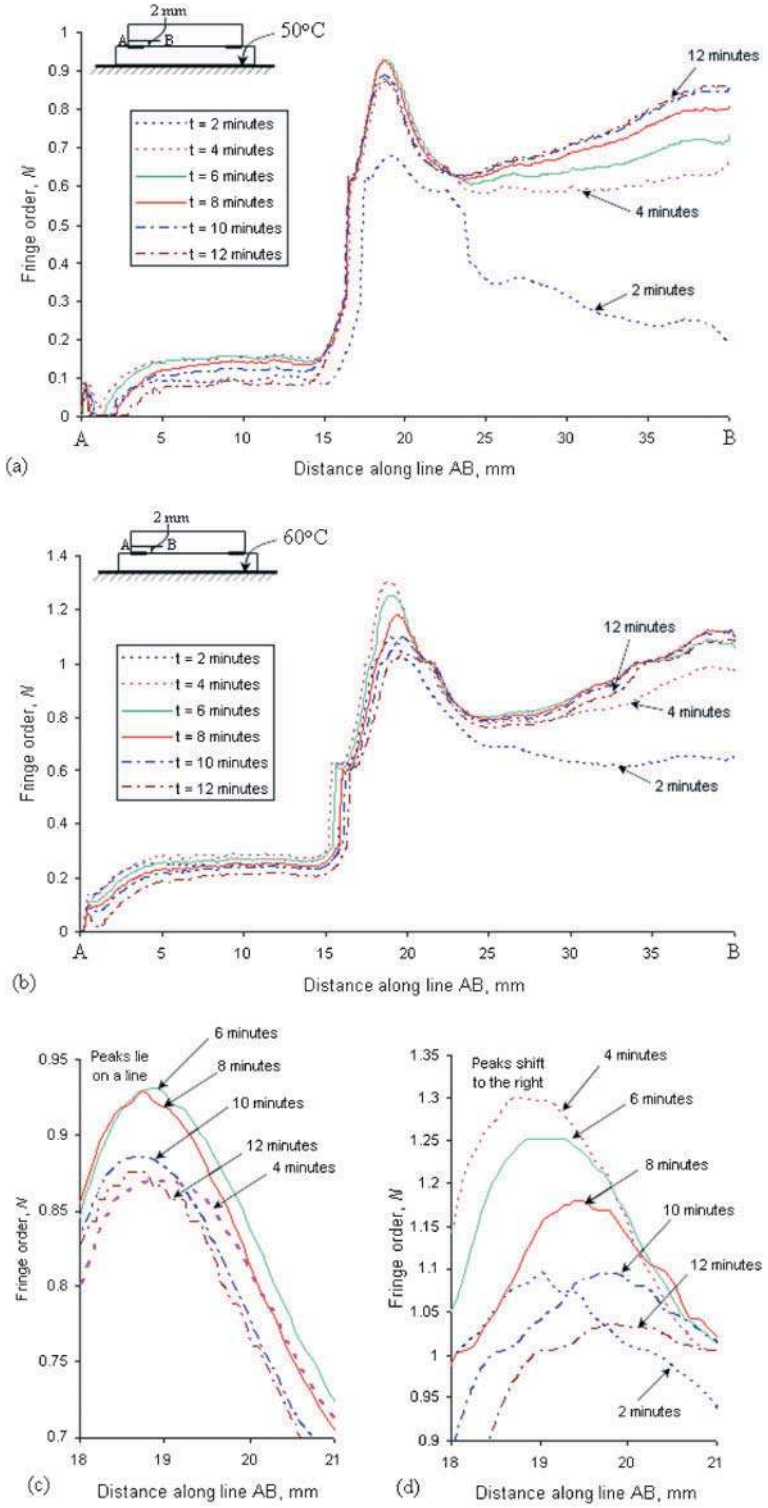

Fig. 9 Fringe order variation along line AB for a few time steps when the bottom face of the aluminium is kept at (a) 50 °C and (b) 60 °C. Zoomed portion of the tile shown in (c) Fig. 9(a) for 50 °C, showing that peaks lie on a line, and (d) Fig. 9(b) for 60 °C, showing that peaks shift to the right

Table 3 Comparison of peak SIF values for various thermal loads

	K_I (MPa $\sqrt{m}$)	K_{II} (MPa $\sqrt{m}$)	$\|K\|$ (MPa $\sqrt{m}$)	Peak value of $\|K\|$ occurring at
Edge heating at 50 °C	0.075	0.03	0.081	6 min 45 s
Edge heating at 60 °C	0.101	0.062	0.119	3 min 30 s
Whole-field convection cooling [**10**]	0.084	0.176	0.195	Steady state

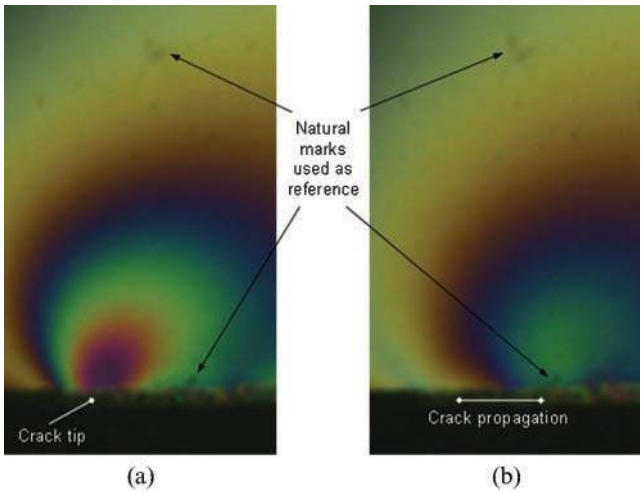

Fig. 10 Zoomed dark-field crack-tip isochromatics for an aluminium–PSM-1 bimaterial specimen kept on a hot plate at 60 °C (a) after 2 min and (b) after 12 min, showing the crack propagation. Reference markings on the specimen are indicated for easy visualization of crack propagation

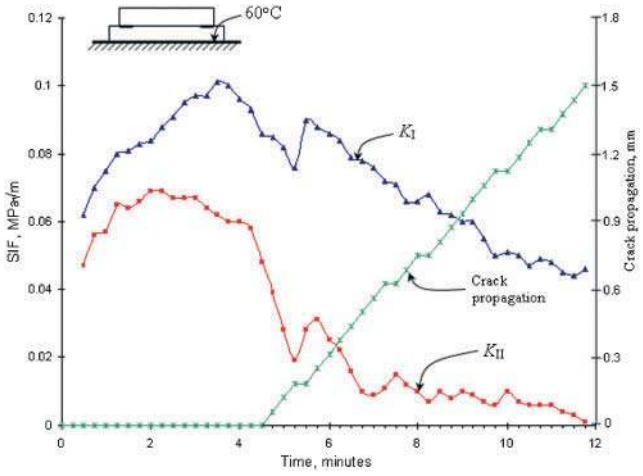

Fig. 11 Graph showing the variation in SIFs for a bimaterial specimen and the crack propagation with time when the bottom face of the aluminium is maintained at 60 °C

4 CONCLUSIONS

In the case of edge heating of bimaterial specimens, the SIFs peak to a high value before steady state and the opening mode is dominant. The SIFs, in particular K_{II}, are found to drop rapidly to very near zero once the crack starts to propagate. The SIF data and crack propagation behaviour recorded in Fig. 11 are valuable for verifying or developing a suitable fracture criterion for crack propagation for this class of problems. A bimaterial crack propagates faster when the opening mode is dominant, and hence, in the design engineering of bimaterial specimens, the mode mixity is to be considered, not just the energy release rate or the modulus of the complex SIF. RTFP with colour adaptation is best suited for the analysis of transient thermal problems because of its capability of single-shot data acquisition and its excellent accuracy.

REFERENCES

1 **Wang, W.-C.** and **Hsu, J.-S.** Re-examination on thermal stresses of bonded structures. *J. Strain Analysis*, 2004, **39**(3), 261–270. DOI: 10.1243/03093240432304268 7.
2 **Wang, W. C.** and **Lin, J. C.** Photoelastic investigation of bimaterial interfacial stresses induced by thermal loading. *Strain*, 2003, **39**, 143–148.
3 **Wang, W. C.** and **Hsu, J. S.** Investigation of analytical solutions for bonded structures by photomechanical methods. *Strain*, 2006, **42**, 107–116.
4 **Tsai, M. Y.** and **Morton, J.** A stress analysis of a thermally loaded bimaterial interface: a localized hybrid analysis. *Mechanics Mater.*, 1992, **13**, 117–130.
5 **Post, D., Wood, J. D., Han, B., Parks, V. J.,** and **Gerstle Jr, F. P.** Thermal stresses in a bimaterial joint: an experimental analysis. *Trans. ASME, J. Appl. Mechanics*, 1994, **61**, 192–198.
6 **Ileri, L.** and **Madenci, E.** Crack initiation and growth in electronic packages. In Proceedings of 45th Electron. Comp. Technol. Conference, Las Vegas, Nevada, 1995, pp. 970–976.
7 **Erdogan, F.** Stress distribution in bonded dissimilar materials with cracks. *Trans. ASME, J. Appl. Mechanics*, 1965, **32**, 403–410.
8 **Brown, E. J.** and **Erdogan, F.** Thermal stress in bonded materials containing cuts on the interface. *Int. J. Fracture*, 1968, **6**, 517–529.
9 **Neethi Simon, B.** and **Ramesh, K.** Numerical and digital photoelastic assessment of bimaterial interfaces in electronic packages. CD Proceedings of ICTACEM, IIT, Kharaghpur, India, 2007.

10 **Neethi Simon, B.** and **Ramesh, K.** Digital photothermoelastic and numerical analysis of transient thermal stresses in cracked bimaterial interfaces. *Trans. ASME, J. Appl. Mech.*, 2009, **76**(4), paper no. 044502.

11 **Kokini, K.** and **Smith, C. C.** Interfacial transient thermal fracture of adhesively bonded dissimilar materials. *Expl Mechanics*, 1989, 312–317.

12 **Ramesh, K.** and **Deshmukh, S. S.** Three fringe photoelasticity – use of colour image processing hardware to automate ordering of isochromatics. *Strain*, 1996, **35**, 79–86.

13 **Madhu, K. R.** and **Ramesh, K.** Noise removal in three-fringe photoelasticity by adaptive colour difference estimation. *Optics and Lasers in Engng*, 2007, **45**, 175–182.

14 **Madhu, K. R., Prasath, R. G. R.,** and **Ramesh, K.** Colour adaptation in three fringe photoelasticity. *Expl Mechanics*, 2007, **47**, 271–276.

15 **Sanford, R. J.** and **Dally, J. W.** A general method for determining mixed mode stress intensity factors. *Engng Fracture Mechanics*, 1972, **4**, 357–366.

16 **Ramesh, K., Gupta, S.,** and **Kelkar, A. A.** Evaluation of stress field parameters in fracture mechanics by photoelasticity – revisited. *Engng Fracture Mechanics*, 1997, **56**, 25–45.

17 **Ravichandran, M.** and **Ramesh, K.** Evaluation of stress field parameters for an interface crack in a bimaterial by digital photoelasticity. *J. Strain Analysis*, 2005, **40**(4), 327–343. DOI: 10.1243/030932405X16034.

18 **Miskioglu, I., Gryzagorides, J.,** and **Burger, C. P.** Material properties in thermal-stress analysis. *Expl Mechanics*, 1980, **21**, 295–301.

19 **Ramesh, K.** *Digital photoelasticity: advanced techniques and applications*, 2000 (Springer-Verlag, Berlin).

20 **Ramesh, K.** Photoelasticity. In *Springer handbook of experimental solid mechanics* (Ed Sharpe Jr, W. N.), 2008, pp. 701–742 (Springer, New York).

21 **Ramji, M.** and **Ramesh, K.** Stress separation in digital phtoelasticity. Part A – Photoelastic data unwrapping and smoothing. *J. Aero. Sci. and Technol.*, 2008, **60**, 5–15.

22 **Deng, X.** General crack-tip fields for stationary and steadily growing interface cracks in anisotropic bimaterials. *Trans. ASME, J. Appl. Mechanics*, 1993, **60**, 183–189.

23 **Senthil Gurunathan, R.** *Digital photoelastic evaluation of stress field parameters for a patched interfacial crack in a bimaterial*, MSc Thesis, IIT Madras, India, 2005.